

**Anomalous magnetic properties of multi-walled carbon nanotubes  
embedded with magnetic nanoparticles: Consistent with  
ultrahigh temperature superconductivity**

Guo-meng Zhao<sup>1,2,\*</sup>, Jun Wang<sup>2</sup>, Yang Ren<sup>3</sup>, and Pieder Beeli<sup>1</sup>

<sup>1</sup> *Department of Physics and Astronomy,  
California State University at Los Angeles,  
Los Angeles, CA 90032, USA*

<sup>2</sup> *Department of Physics,  
Faculty of Science, Ningbo University,  
Ningbo, P. R. China*

<sup>3</sup> *X-Ray Science Division,  
Advance Photon Source,  
Argonne National Laboratory,  
Argonne, IL 60439, USA*

arXiv:1106.4323v2 [cond-mat.str-el] 19 Jul 2011

## Abstract

We report high-temperature (300-1120 K) magnetization data of Fe and Fe<sub>3</sub>O<sub>4</sub> nanoparticles embedded in multi-walled carbon nanotubes. The magnetic impurity concentrations are precisely determined by both high-energy synchrotron x-ray diffractometer and inductively coupled plasma mass spectrometer. We unambiguously show that the magnetic moments of Fe and Fe<sub>3</sub>O<sub>4</sub> nanoparticles are enhanced by a factor of about 3 compared with what they would be expected to have for free (unembedded) magnetic nanoparticles. The magnetization enhancement factor is nearly independent of the applied magnetic field but depends significantly on the cooling rate. What is more intriguing is that the enhanced moments were completely lost when the sample was heated up to 1120 K and the lost moments at 1120 K were completely recovered through several thermal cycles below 1020 K. Furthermore, there is a rapid increase or decrease in the magnetization below about 60 K. The anomalous magnetic properties cannot be explained by existing physics models except for the paramagnetic Meissner effect due to the existence of ultrahigh temperature superconductivity in the multi-walled carbon nanotubes.

## I. INTRODUCTION

Graphene is a sheet of carbon atoms distributed in a honeycomb lattice and is the building block for graphite and carbon nanotubes. Originating from conical valence and conduction bands that meet at a single point in momentum space, the massless charge carriers of graphene, known as Dirac fermions, exhibit relativistic behavior. Strong electron-electron correlation of the Dirac fermions in graphene can lead to the formation of a short-range resonating-valence-bond (RVB) liquid<sup>1</sup> and/or to a ferromagnetic instability<sup>2</sup>. On the basis of the RVB theory of superconductivity originally proposed by Anderson<sup>3</sup>, heavily doped graphene can exhibit ultrahigh temperature ( $\sim 5000$  K) *d*-wave superconductivity<sup>4</sup>. These theoretical works appear to agree with experimental observations of the intrinsic high-temperature ferromagnetism in graphite and carbon-based materials<sup>5–10</sup> and possible high-temperature superconductivity in carbon films<sup>11,12</sup>, highly oriented pyrolytic graphite<sup>5,13</sup>, carbon nanotubes<sup>14–16</sup>, and amorphous carbon<sup>17</sup>. In addition, a giant magnetization enhancement has recently been identified in nickel nanoparticles embedded in multi-walled carbon nanotubes (MWCNTs)<sup>18</sup>. The giant magnetization enhancement was tentatively explained in terms of ultrahigh temperature superconductivity in MWCNTs<sup>18</sup>.

Here we report high-temperature (300–1120 K) magnetization data of Fe and Fe<sub>3</sub>O<sub>4</sub> nanoparticles embedded in multi-walled carbon nanotubes. Similar to the previous finding for nickel nanoparticles<sup>18</sup>, we unambiguously show that the magnetic moments of Fe and Fe<sub>3</sub>O<sub>4</sub> nanoparticles are also enhanced by a factor of about 3. The magnetization enhancement factor is nearly independent of the applied magnetic field but depends significantly on the cooling rate. What is more intriguing is that the enhanced moments were completely lost when the sample was heated up to 1120 K and the lost moments at 1120 K were completely recovered through several thermal cycles below 1020 K. Furthermore, there is a rapid increase or decrease in the magnetization below about 60 K. The anomalous magnetic properties cannot be explained by existing physics models except for the paramagnetic Meissner effect due to the existence of ultrahigh temperature superconductivity in the multi-walled carbon nanotubes.

## II. EXPERIMENTS

MWCNT mat samples embedded with Fe and Fe<sub>3</sub>O<sub>4</sub> nanoparticles were obtained from SES Research of Houston (Catalog No. RS0657). The mat samples were synthesized by chemical vapor deposition under catalyzation of Fe nanoparticles. During the purification process, some Fe nanoparticles were oxidized into the Fe<sub>3</sub>O<sub>4</sub> and  $\alpha$ -Fe<sub>2</sub>O<sub>3</sub> phases and were removed by HCl. As confirmed by high-energy synchrotron x-ray diffraction (XRD) data (see Fig. 2 below), some fractions of Fe, Fe<sub>3</sub>O<sub>4</sub>, and  $\alpha$ -Fe<sub>3</sub>O<sub>4</sub> nanoparticles still remain due to incomplete purification. The metal-based impurity concentrations of the mat sample were also determined by a Perkin-Elmer Elan-DRCe inductively coupled plasma mass spectrometer (ICP-MS), which yielded the metal-based magnetic impurity concentrations by weight: Fe = 0.69%, Co = 0.0036%, Ni = 0.0021%.

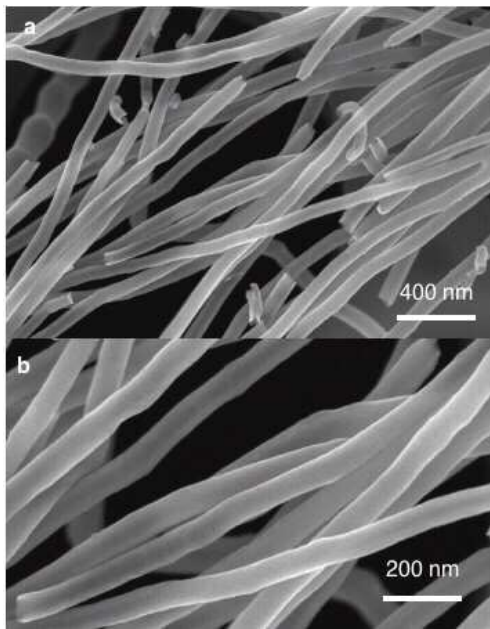


FIG. 1: Scanning electron microscopy (SEM) images of the MWCNT mat sample. The tubes are quite uniform and their mean outer diameter is about 70 nm.

The morphology of the mat sample can be checked from scanning electron microscopy (SEM) images shown in Fig. 1. The SEM images were taken by a field emission scanning electron microscopy (FE-SEM, Hitachi S-4800) using an accelerating voltage of 3 kV. One can see that the tubes are quite uniform and their mean outer diameter is about 70 nm.

Since the magnetic impurity phases in the MWCNT sample are so minor, it is impossible to identify the minor phases from a normal low-energy x-ray diffraction (XRD) spec-

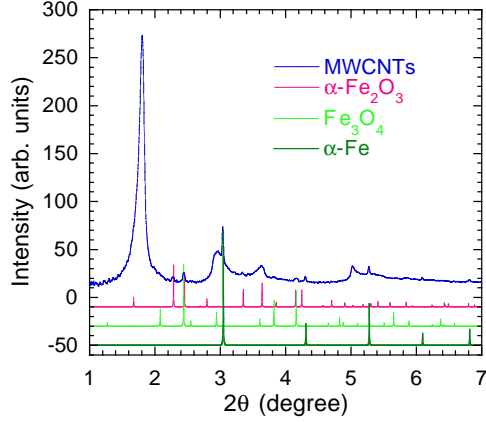


FIG. 2: High-energy synchrotron x-ray diffraction spectrum of a virgin MWCNT mat sample along with the standard spectra of  $\alpha$ -Fe,  $\text{Fe}_3\text{O}_4$ , and  $\alpha$ - $\text{Fe}_2\text{O}_3$  phases. Quantitative analyses of the XRD spectrum (see below) show that the sample contains  $0.241 \pm 0.004\%$  (by weight) of Fe,  $0.216 \pm 0.015\%$  of  $\alpha$ - $\text{Fe}_2\text{O}_3$ , and  $0.250 \pm 0.010\%$  of  $\text{Fe}_3\text{O}_4$  and that the mean diameters of Fe,  $\alpha$ - $\text{Fe}_2\text{O}_3$ , and  $\text{Fe}_3\text{O}_4$  nanoparticles are 46, 23, and 18 nm, respectively.

trum. But we can precisely determine magnetic impurity concentrations from high-energy synchrotron x-ray diffraction data<sup>18</sup>. Fig. 2 shows a synchrotron XRD spectrum for the MWCNT sample along with the standard spectra of  $\alpha$ -Fe,  $\text{Fe}_3\text{O}_4$ , and  $\alpha$ - $\text{Fe}_2\text{O}_3$  phases. Using monochromated radiation with a wavelength of  $\lambda = 0.1078 \text{ \AA}$ , the XRD spectrum was taken on a high-energy synchrotron x-ray beam-line 11-ID-C at the Advanced Photon Source, Argonne National Laboratory. In addition to the major peaks corresponding to the diffraction peaks of MWCNTs<sup>19</sup>, there are many minor peaks, which match well with all the peaks of the  $\alpha$ -Fe,  $\text{Fe}_3\text{O}_4$ , and  $\alpha$ - $\text{Fe}_2\text{O}_3$  phases. This indicates that the visible impurity phases are  $\alpha$ -Fe,  $\text{Fe}_3\text{O}_4$ , and  $\alpha$ - $\text{Fe}_2\text{O}_3$ , in agreement with the impurity analysis using the ICP-MS above.

In Fig. 3a, we display the expanded view of the MWCNT (002) peak for this sample. The solid red line in Fig. 3a is the fitted curve by the sum of a Gaussian and a cut-off Lorentzian function, which takes into account both domain size broadening and strain broadening<sup>19</sup>. The Lorentzian function is cut off to zero when  $|2\theta - 2\theta_0| \geq 3.65\gamma$ , where  $2\theta_0$  is the peak position and  $\gamma$  is the full width at half maximum (FWHM). This cut-off Lorentzian function plus a Gaussian function can excellently fit the MWCNT (002) peak of Ref.<sup>19</sup>.

Figure 3b shows the expanded view of the Fe (211) peak of sample RS0657. The solid red line is the fitted curve by a Gaussian function. The Gaussian function is consistent

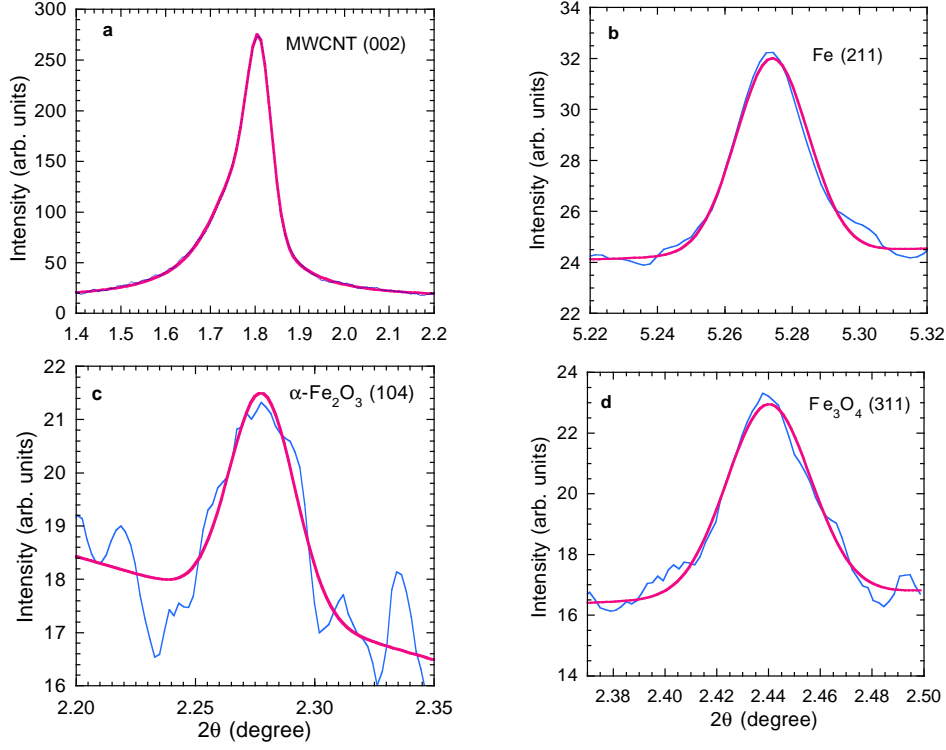


FIG. 3: a) The expanded view of the MWCNT (002) peak. b) The expanded view of the Fe (211) peak. c) The expanded view of the  $\alpha$ -Fe<sub>2</sub>O<sub>3</sub> (104) peak. d) The expanded view of the Fe<sub>3</sub>O<sub>4</sub> (311) peak.

with particle-size broadening<sup>19</sup>. The integrated intensity of the Fe (211) peak is found to be  $0.206 \pm 0.004\%$  of the intensity of the MWCNT (002) peak. Using the standard intensities of graphite's (002) peak and Fe (211) peak and assuming that the intensity of MWCNT (002) peak is the same as that of graphite (002) peak, we find that the ferromagnetic Fe concentration is  $0.241 \pm 0.004\%$  (by weight).

Figures 3c and 3d display the expanded views of the  $\alpha$ -Fe<sub>2</sub>O<sub>3</sub> (104) and Fe<sub>3</sub>O<sub>4</sub> (311) peaks, respectively. The solid red line in Fig. 3c is the fitted curve by a Gaussian function. The integrated intensity of the  $\alpha$ -Fe<sub>2</sub>O<sub>3</sub> (104) peak is found to be  $0.348 \pm 0.024\%$  of the intensity of the MWCNT (002) peak. From the intensity ratio, we find that the  $\alpha$ -Fe<sub>2</sub>O<sub>3</sub> concentration is  $0.216 \pm 0.015\%$ .

The spectrum of the Fe<sub>3</sub>O<sub>4</sub> (311) peak in Fig. 3d is obtained by subtracting the expected  $\alpha$ -Fe<sub>2</sub>O<sub>3</sub> (110) peak [whose integrated intensity is 76% of that for the  $\alpha$ -Fe<sub>2</sub>O<sub>3</sub> (104) peak] from the raw spectrum. The solid red line in Fig. 3d is the fitted curve by a Gaussian function. The integrated intensity of the Fe<sub>3</sub>O<sub>4</sub> (311) peak is found to be  $0.647 \pm 0.020\%$  of the intensity of the MWCNT (002) peak. From the intensity ratio, we find that the Fe<sub>3</sub>O<sub>4</sub>

concentration is  $0.250\pm 0.010\%$ .

The quantitative analyses of the XRD spectrum show that the sample contains  $0.241\pm 0.004\%$  of Fe,  $0.216\pm 0.015\%$  of  $\alpha\text{-Fe}_2\text{O}_3$ , and  $0.250\pm 0.010\%$  of  $\text{Fe}_3\text{O}_4$ . These impurity phases contribute to a metal-based Fe concentration of  $0.58\pm 0.02\%$ , which is about  $0.11\pm 0.04\%$  lower than the total Fe concentration ( $0.69\pm 0.02\%$ ) determined from the ICP-MS. Below we shall attribute this  $0.11\pm 0.04\%$  discrepancy—which is not visible in the XRD spectrum but can be clearly seen in magnetization data—to a minor phase of  $\text{Fe}_3\text{C}$ .

We can determine mean diameters of magnetic nanoparticles from the XRD peak widths. For the  $\text{Fe}_3\text{O}_4$  (311) peak, the full width at half maximum  $\gamma = 0.0382(1)^\circ$ . Using the Scherrer equation:  $d = 0.89\lambda/(\gamma_b \cos \theta)$  and with  $\gamma_b = 0.0312^\circ$  (after correcting for the instrumental broadening  $\gamma_i = 0.0221^\circ$ ), we calculate  $d = 18$  nm. Similarly, the mean diameters of  $\alpha\text{-Fe}_2\text{O}_3$  and Fe nanoparticles are evaluated to be 23 and 46 nm, respectively.

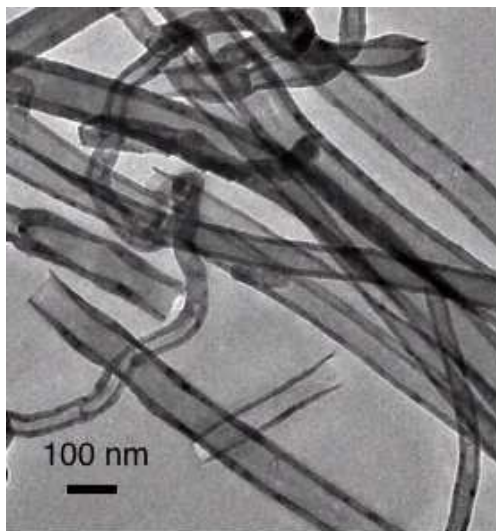


FIG. 4: Transmission electron microscopic (TEM) image of the MWCNTs, which was recorded by FEI Tecnai F20 with an accelerating voltage of 200 kV.

There are two ways to determine the mean inner diameter of the MWCNTs. Scanning tunneling microscopic images shown in Fig. 1 indicate that the mean outer diameter of the tubes is about 70 nm. Using the Scherrer equation, the mean wall thickness of the MWCNTs is determined to be about 9 nm from the FWHM value of the Gaussian function obtained by fitting the MWCNT (002) peak above. Therefore, the mean inner diameter of the MWCNTs is about 50 nm, close to the mean diameter of the Fe nanoparticles. This is consistent with the transmission electron microscopic (TEM) image shown in Fig. 4. The TEM image also

indicates that the mean wall thickness of the MWCNTs is about 10 nm, in agreement with the XRD result.

Figure 5 shows zero-field-cooled (ZFC) and field-cooled (FC) susceptibilities for a virgin sample of RS0657. Magnetic moment was measured using a Quantum Design vibrating sample magnetometer (VSM). The absolute measurement uncertainties in temperature and moment are less than 20 K and  $1 \times 10^{-6}$  emu, respectively. The sample was first heated up to 1000 K and cooled down to 320 K in a “zero” ( $< 0.06$  Oe) field. A magnetic field of 0.5 Oe was applied at 320 K and the ZFC susceptibility was measured upon warming up to 1000 K. The FC susceptibility was taken when the temperature was lowered from 1000 K to 320 K. The FC and ZFC susceptibility data clearly show a magnetic transition at about 850 K, which is associated with the ferrimagnetic transition of the  $\text{Fe}_3\text{O}_4$  impurity phase. There is also a second magnetic transition at about 480 K, which corresponds to the ferromagnetic transition of the  $\text{Fe}_3\text{C}$  impurity phase.

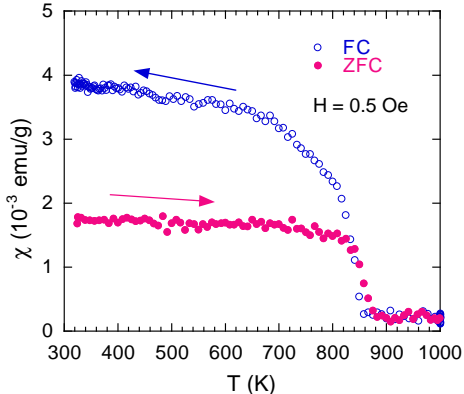


FIG. 5: Zero-field-cooled (ZFC) and field-cooled (FC) susceptibility data for a virgin MWCNT sample of RS0657. The FC and ZFC susceptibilities clearly show a magnetic transition at about 850 K, which is associated with the ferrimagnetic transition of the  $\text{Fe}_3\text{O}_4$  impurity phase. There is also a second magnetic transition at about 480 K, which corresponds to the ferromagnetic transition of the  $\text{Fe}_3\text{C}$  impurity phase.

Figure 6 shows magnetic hysteresis loops at 315 K and 910 K for sample RS0657, respectively. The linear field dependence of the magnetization with a negative slope at  $H > 10$  kOe is due to the diamagnetic contribution. The linear extrapolation to  $H = 0$  yields  $M_s = 1.66$  emu/g at 315 K and  $M_s = 0.62$  emu/g at 910 K. The temperature dependence of the saturation magnetization is displayed in Fig. 7a. From the magnetic hysteresis loops, we also determine the coercive field  $H_C$ , which is summarized in Fig. 7b. It is interesting that



$H_C$  is negligibly small above 840 K, in agreement with a negligible remanent magnetization above 840 K (see Fig. 8a). Another remarkable feature is that the remanent magnetization is almost reversible between 315 and 910 K (see Fig. 8b).

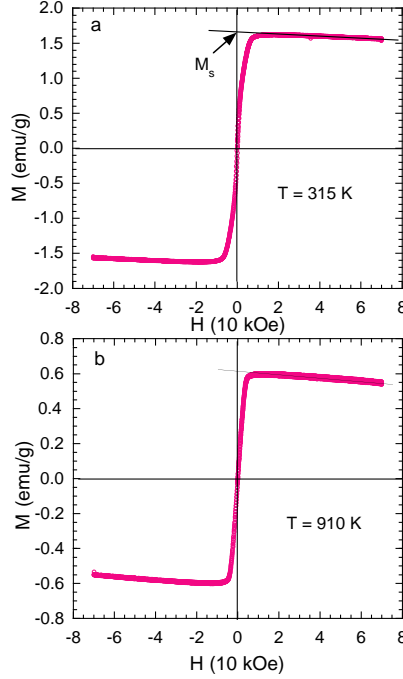


FIG. 6: a) Magnetic hysteresis loop at 315 K for the MWCNT sample. b) Magnetic hysteresis loop at 910 K for the MWCNT sample.

From the hysteresis loops, we can also determine the initial low-field susceptibility  $\chi_i$  from the linear field dependence of the magnetization below 200 Oe. We find that  $\chi_i = 5.0 \times 10^{-4}$  emu/g at 300 K and  $\chi_i = 1.9 \times 10^{-4}$  emu/g at 910 K. It is known that the initial low-field susceptibility only depends on the demagnetization factor for strong ferromagnets such as Fe and  $\text{Fe}_3\text{O}_4$ . For spherical particles with a demagnetization factor of  $1/3$ ,  $\chi_i = 3/4\pi$  emu/cm<sup>3</sup> = 0.239 emu/cm<sup>3</sup>. At 910 K, only the Fe impurity phase contributes the initial susceptibility, which would be  $7.35 \times 10^{-5}$  emu/g if the 0.24% Fe nanoparticles were decoupled from the MWCNTs. Therefore, the initial susceptibility of the embedded Fe nanoparticles is enhanced by a factor of 2.6 compared with what they would be expected to have if they would be isolated from the MWCNTs. For  $\text{Fe}_3\text{O}_4$  nanoparticles with the concentration of 0.25%, the expected initial susceptibility would be  $1.2 \times 10^{-4}$  emu/g, which is also a factor of 2.6 smaller than the measured difference ( $3.1 \times 10^{-4}$  emu/g) between the susceptibilities at 300 K and 910 K.

Figure 9a shows temperature dependencies of the high-field (10 kOe) magnetizations for

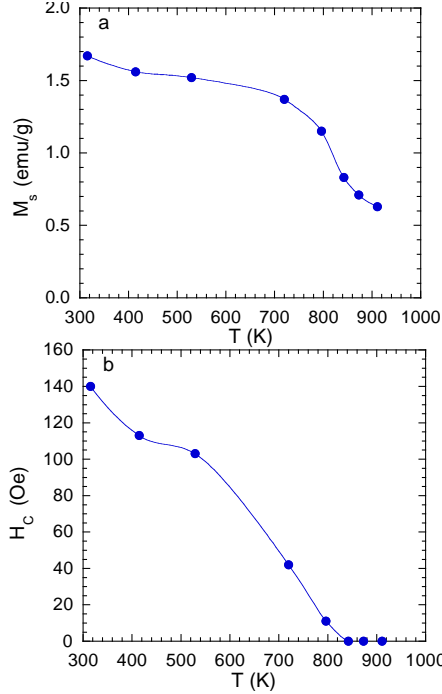


FIG. 7: a) Temperature dependence of the saturation magnetization  $M_s$ . b) Temperature dependence of the coercive field  $H_C$ .

another virgin MWCNT sample of RS0657. Since the magnetization in 10 kOe is close to the saturation magnetization (see Fig. 6), the temperature dependence of the saturation magnetization is approximated by the temperature dependence of the magnetization in 10 kOe. The first warm-up magnetization curve clearly demonstrates three magnetic transitions at about 500 K, 860 K, and 1060 K, which should be associated with the phases of the magnetic  $\text{Fe}_3\text{C}$ ,  $\text{Fe}_3\text{O}_4$ , and  $\alpha\text{-Fe}$  ( $T_C = 1047$  K), respectively. The slightly higher magnetic transition temperatures than the expected ones are due to a thermal lag.

One can clearly see that the thermal hysteresis of the high-field magnetization is anomalous. When the sample was cooled from 1120 K, the cool-down magnetization was reduced dramatically compared with the first warm-up magnetization. After two more thermal cycles below 1020 K, the lost magnetization at 1120 K was recovered almost completely.

In Fig. 9b, we decompose the high-field magnetization ( $\simeq M_s$ ) into contributions from the  $\alpha\text{-Fe}$  and  $\text{Fe}_3\text{O}_4$  impurity phases on the assumption that  $M_s(t)/M_s(0)$  for both Fe and  $\text{Fe}_3\text{O}_4$  impurity phases is the same as that for free (unembedded)  $\alpha\text{-Fe}$  nanoparticles (where  $t = T/T_C$ ). The  $M_s(t)/M_s(0)$  curve for unembedded  $\alpha\text{-Fe}$  nanoparticles with the mean diameter of over 100 nm was also measured in a field of 10 kOe. The solid blue line is the contribution from the Fe impurity phase with  $M_s(300\text{K}) = 0.96$  emu/g and the solid green

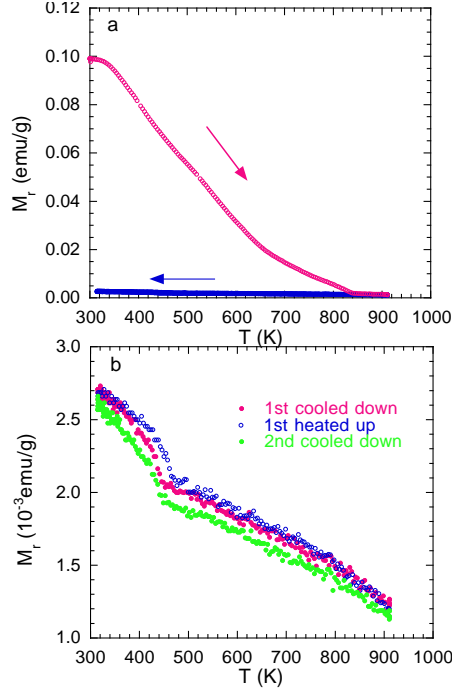


FIG. 8: a) Temperature dependence of the initial remanent magnetization. The remanent magnetization was measured in a field of less than 0.03 Oe after the sample was magnetized in a magnetic field of 70 kOe at 300 K. b) Thermal hysteresis of the remanent magnetization between 315 and 910 K.

line is the contribution from the  $\text{Fe}_3\text{O}_4$  impurity phase with  $M_s(300\text{K}) = 0.46$  emu/g. The remaining  $M_s(300\text{K}) = 0.18$  emu/g should contribute from the  $\text{Fe}_3\text{C}$  impurity phase.

For unembedded Fe nanoparticles with a mean diameter of 46 nm, the saturation magnetization can be extrapolated to be 160 emu per gram of Fe from the measured diameter dependence of  $M_s(300\text{K})$  (Ref.<sup>20</sup>). Using the Fe concentration of 0.24%,  $M_s(300\text{K})$  is calculated to be 0.38 emu/g if the Fe nanoparticles would be isolated from the MWCNTs. This clearly indicates that the saturation magnetization (0.96 emu/g) of the 46-nm Fe nanoparticles embedded in MWCNTs is enhanced by a factor of about 2.5 compared with that (0.38 emu/g) of the unembedded Fe nanoparticles. This magnetization enhancement factor is very close to that (2.6) found above from the initial low-field magnetization. This indicates that the magnetization enhancement factor is nearly independent of the magnetic field.

For unembedded  $\text{Fe}_3\text{O}_4$  nanoparticles with a mean diameter of 18 nm, the  $M_s(300\text{K})$  value can be inferred to be about 62 emu per gram of  $\text{Fe}_3\text{O}_4$  from the measured diameter dependence of  $M_s(300\text{K})$  (Ref.<sup>21</sup>). With the  $\text{Fe}_3\text{O}_4$  concentration of 0.25%, we calculate  $M_s(300\text{K})$  to be 0.155 emu/g if the  $\text{Fe}_3\text{O}_4$  nanoparticles would be isolated from the MWC-

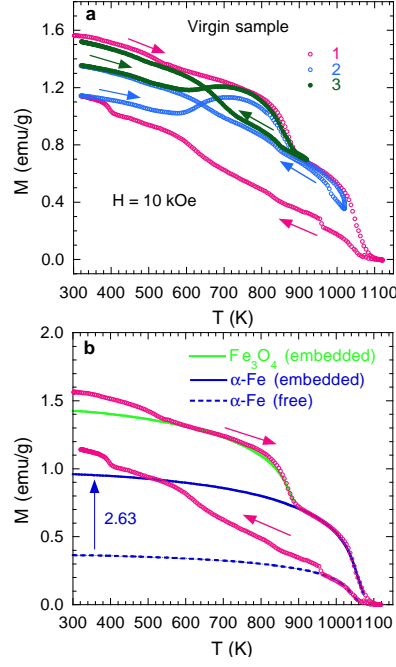


FIG. 9: a) Temperature dependencies of the high-field magnetizations for a virgin MWCNT sample of RS0657, which were measured in a magnetic field of 10 kOe. There are three thermal cycles, labeled by 1, 2 and 3. b) Magnetic decomposition into contributions from the  $\alpha$ -Fe and  $\text{Fe}_3\text{O}_4$  impurity phases. The solid blue and green lines are the contribution from the Fe and  $\text{Fe}_3\text{O}_4$  impurity phases, respectively. The dashed blue line is the expected contribution from the unembedded 46-nm Fe nanoparticles with the concentration of 0.23% (very close to  $0.241 \pm 0.004\%$  determined from the XRD data).

NTs. It is clear that the  $M_s(300\text{K})$  value (0.46 emu/g) of the 18-nm  $\text{Fe}_3\text{O}_4$  nanoparticles embedded in MWCNTs is enhanced by a factor of about 3.0 compared with that (0.155 emu/g) of the unembedded  $\text{Fe}_3\text{O}_4$  nanoparticles. This magnetization enhancement factor is similar to that for 11-nm nickel nanoparticles<sup>18</sup>.

The dashed blue line in Fig. 9b is the expected magnetization curve for unembedded Fe nanoparticles with the mean diameter of 46 nm and the concentration of 0.23% (very close to  $0.241 \pm 0.004\%$  determined from the XRD data). This curve matches very well with the first cool-down magnetization data between 960 and 1060 K. This implies that the enhanced magnetization was completely lost at 1120 K and not recovered upon cooling down to 960 K. This result vividly demonstrates that the Fe impurity concentration determined from the XRD data is precise. By comparing the solid blue line to the dashed blue line, we find the magnetization enhancement factor to be 2.63. This parameter-free determination of

the magnetization enhancement factor justifies our XRD analyses and provides indisputable evidence for the giant magnetization enhancement of magnetic nanoparticles embedded in MWCNTs.

It is interesting that in the first cool-down curve there are two sharp increases in the magnetization at about 960 K and 400 K. There are also two gradual increases at about 860 K and 660 K. The small magnetization increase (about 0.1 emu/g) at 860 K would be expected for the ferrimagnetic transition of the  $\text{Fe}_3\text{O}_4$  impurity phase if they would be isolated from the MWCNTs. This suggests that the enhanced magnetization of the  $\text{Fe}_3\text{O}_4$  impurity phase seen in the first warm-up magnetization data was also lost upon heating up to 1120 K. In fact, the enhanced magnetization of the  $\text{Fe}_3\text{O}_4$  impurity phase was lost almost completely at 920 K, as seen from curve 3 in Fig. 9a. The lost magnetization of the Fe phase was partially gained back at 960 K. The lost magnetizations of both  $\text{Fe}_3\text{O}_4$  and Fe phases were completely recovered through two more thermal cycles below 1020 K (see Fig. 9a). It is striking that—independent of whether the sample is heated or cooled—the significant magnetization gain always occurs in the temperature region between 600 and 700 K.

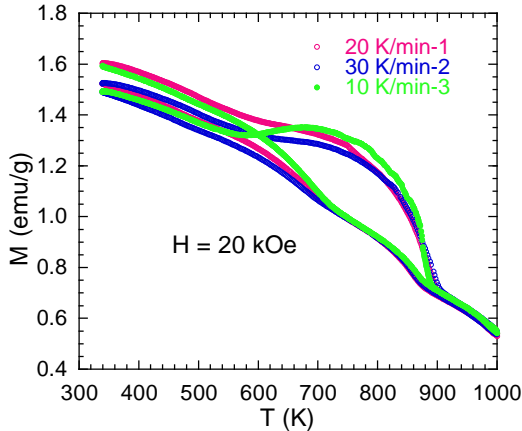


FIG. 10: Temperature dependencies of the magnetizations measured with different heating/cooling rates.

In Fig. 10, we plot the temperature dependencies of the magnetizations, which were measured in a magnetic field of 20 kOe and with different heating/cooling rates. Fig. 10 indicates that the cool-down magnetizations below 720 K depend significantly on the cooling rates; the slower the cooling rate is, the larger the magnetization is. The cooling-rate dependence of the cool-down magnetization is another unusual magnetic property of our samples.

Figure 11a shows low-temperature susceptibility curves measured in a magnetic field of 1 kOe. From the first cool-down curve, one can see that the susceptibility drops sharply at  $T_{on} = 40$  K, reaches a minimum value at  $T_d = 28$  K, and increases rapidly as the temperature is further reduced. Upon warming, the susceptibility does not follow the cool-down curve; both  $T_{on}$  and  $T_d$  shift to higher temperatures and the susceptibility value at  $T_d$  becomes much smaller. One more thermal cycle leads to a small increase in  $T_{on}$  and a large drop in the susceptibility below 40 K. Furthermore, the susceptibilities below  $T_{on}$  show a large fluctuation, suggesting a metastable magnetic state.

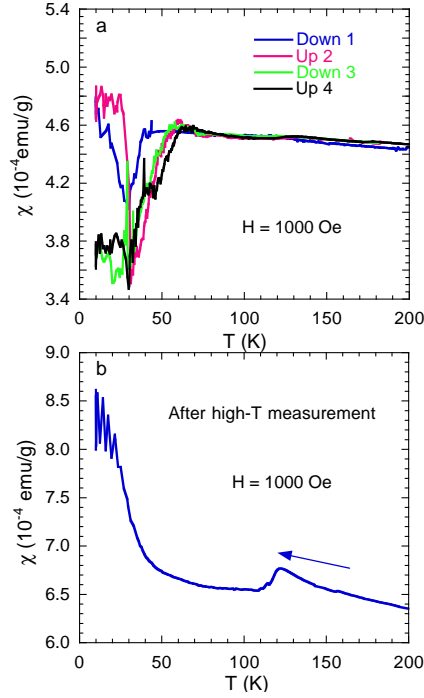


FIG. 11: a) Low-temperature susceptibility curves measured in a magnetic field of 1 kOe. b) Low-temperature susceptibility curve after high-temperature susceptibility data were taken.

It is remarkable that low-temperature magnetic behavior changed dramatically after high-temperature susceptibility measurement were done (see Fig. 11b). The susceptibility does not drop but increases sharply at  $T_{on}$ . A sharp drop at about 122 K is associated with the Verwey transition of the  $\text{Fe}_3\text{O}_4$  impurity phase.

### III. DISCUSSION

Now we discuss possible explanations to the observed anomalous magnetic properties of multi-walled carbon nanotubes embedded with magnetic nanoparticles. Firstly, we would

like to check if the magnetic impurity phases identified from the high-energy XRD spectrum and ICP-MS can explain the data. It is known that high-field magnetizations for ferromagnetic/ferrimagnetic materials have negligible thermal hysteresis due to the fact that the magnetic field is large enough to saturate the magnetization. Indeed, we have demonstrated that the high-field (10 kOe) magnetization of pure  $\text{Fe}_3\text{O}_4$  nanoparticles has a negligible thermal hysteresis<sup>22</sup>. Therefore, the observed anomalous thermal hysteresis of the high-field magnetization cannot be explained by ferrimagnetic thermal hysteresis of  $\text{Fe}_3\text{O}_4$  nanoparticles or ferromagnetic thermal hysteresis of Fe nanoparticles.

If we assume that the spin order of  $\text{Fe}_3\text{O}_4$  nanoparticles is not independent of the spin order of Fe nanoparticles, the frustration effect arising from the competition between the interactions of the two types of nanoparticles may lead to the aging effect, memory, and rejuvenation effect, which may account for the anomalous thermal hysteresis in the total magnetization. If this scenario could explain the anomalous thermal hysteresis below the Curie temperature (850 K) of the  $\text{Fe}_3\text{O}_4$  impurity phase, it could not consistently explain the anomalous thermal hysteresis above 850 K where  $\text{Fe}_3\text{O}_4$  is paramagnetic and Fe is the only ferromagnetic phase. Furthermore, this scenario cannot consistently explain the giant moment enhancement. This is because the saturation magnetization of an Fe-core/ $\text{Fe}_3\text{O}_4$ -shell particle is a simple superposition of the  $M_s$  contributions from Fe and  $\text{Fe}_3\text{O}_4$  (see Ref.<sup>23</sup>).

Another possibility is that the magnetism of  $\text{Fe}_3\text{O}_4$  nanoparticles may be related to the superparamagnetism. In this case, all the spins in each nanoparticle are ordered at high temperatures. With decreasing temperature the spin direction of nanoparticles may be frozen, forming either a superparamagnet or a superspin glass. The anomalous memory effect due to the spin frustration may be associated with the anomalous thermal hysteresis. This possibility is unlikely because of the following reasons. Firstly, our  $\text{Fe}_3\text{O}_4$  nanoparticles are not superparamagnetic because the coercive field and remanent magnetization are nonzero before the Curie temperature is reached, as seen from Fig. 7b and Fig. 8a. Secondly, it is known that the saturation magnetization of the superparamagnetic nanoparticles is always reduced compared with the bulk value, in contrast to the giant enhancement. Thirdly, our magnetic data for pure 12-nm  $\text{Fe}_3\text{O}_4$  nanoparticles<sup>22</sup> do not show sizable thermal hysteresis.

Since the identified magnetic impurity phases cannot explain the data, we then shall consider interplay between the magnetic nanoparticles and the MWCNTs. We have shown that<sup>18</sup> the giant magnetic moment enhancement of nickel nanoparticles embedded in MWC-

NTs is unlikely to arise from the magnetic proximity effect<sup>24</sup>. For the case of 11-nm nickel nanoparticles embedded in MWCNTs<sup>18</sup>, the induced moment  $m$  per contact carbon within this magnetic proximity model was calculated to be  $5.1 \mu_B$  (where  $\mu_B$  is Bohr magneton). Similarly we calculate  $m = 61 \mu_B$  for 46-nm Fe nanoparticles embedded in MWCNTs and  $m = 8.0 \mu_B$  for 18-nm  $\text{Fe}_3\text{O}_4$  nanoparticles embedded in MWCNTs. Within the density function theory<sup>24</sup>, the induced moment per contact carbon is calculated to be about  $0.1 \mu_B$ , which is too small to explain the observed giant moment enhancements. Another difficulty with this scenario is that it cannot explain the anomalous thermal hysteresis of the high-field magnetization and no observable changes in the Curie temperatures of the nanoparticles.

It is possible that a strong diamagnetic tube could enhance the extrinsic magnetic moment of a (single-domain) magnet embedded inside it. If the tube were a perfect diamagnet, the “poles” of the magnet would be extended further apart (to the length of the tube) without changing their strength, thus giving an extrinsic enhancement to the magnetic moment. This is because the perfect diamagnetism of the tube prevents the magnetic field lines of the magnet from leaking out through the wall of the tube. The plausibility of this interpretation depends on whether MWCNTs would exhibit strong diamagnetism when the magnetic field is applied in the tube-axis direction. Since the orbital diamagnetism for the field parallel to the tube-axis direction is negligibly small, the strong diamagnetism could arise from superconductivity or ideal conductivity due to ballistic transport.

If the strong diamagnetism along the tube axes exists in the MWCNTs due to ballistic transport, the magnetizations of the magnetic nanoparticles embedded inside innermost shells of the MWCNTs can be enhanced when the magnetic field is applied at a temperature below a critical temperature  $T_b$  where the ballistic transport disappears. The enhanced magnetizations should get lost above  $T_b$  due to the disappearance of the strong diamagnetism. Curves 3 and 1 in Fig. 9a imply that the enhanced magnetization of the  $\text{Fe}_3\text{O}_4$  nanoparticles gets lost at 920 K while the enhanced magnetization of the Fe nanoparticles remains at this temperature and gets lost at 1120 K. This would imply two distinctive  $T_b$ 's in the MWCNTs, which happen to coincide with the Curie temperatures of the  $\text{Fe}_3\text{O}_4$  and Fe phases. This is unlikely. More serious problem with this scenario is that, unlike a superconductor, there is no diamagnetism and thus no magnetization enhancement when the sample is cooled down from a temperature above  $T_b$ . This is in sharp contrast to what we have observed.

If the strong diamagnetism along the tube axes exists in the MWCNTs due to super-



conductivity, the magnetization enhancement is always possible below the superconducting transition temperature  $T_c$  independent of whether the field is applied at a temperature above or below  $T_c$ . In order for this interpretation to be valid, one must assume that there would be two distinctive  $T_c$ 's in the MWCNTs, which are close to the Curie temperatures of the  $\text{Fe}_3\text{O}_4$  and Fe phases. This is also unlikely. Therefore, the diamagnetic Meissner effect in superconducting MWCNTs should be very weak. Indeed, the small diamagnetic Meissner effect along the tube axes has been identified for pure MWCNTs and the magnitude of the diamagnetic Meissner effect is found to be in quantitative agreement with the inferred magnetic penetration depth from the measured carrier concentration<sup>16</sup>. The very weak diamagnetic Meissner effect in the MWCNTs is simply because the magnetic penetration depth is significantly larger than the wall thicknesses of the tubes.

Finally, the giant magnetization enhancement, the anomalous thermal hysteresis of the high-field magnetization, and the unusual cooling-rate dependence of the high-field magnetization can be naturally explained in terms of the high-field paramagnetic Meissner effect (HFPME) due to the existence of ultrahigh temperature superconductivity in the MWCNTs. The HFPME has been observed in large crystals<sup>26</sup> and melt-textured samples<sup>27</sup> of  $\text{YBa}_2\text{Cu}_3\text{O}_{7-y}$ , which was attributed to field-induced flux pinning (a “fishtail” effect)<sup>26</sup>. The field-induced flux pinning can be enhanced by inclusion of magnetic impurity phases, as in the case of the melt-textured samples<sup>27</sup> of  $\text{YBa}_2\text{Cu}_3\text{O}_{7-y}$ , which contain a paramagnetic impurity phase of  $\text{Y}_2\text{BaCuO}_5$ . The HFPME causes an apparent increase of the paramagnetic magnetization of the impurity phase (due to flux trapping on the paramagnetic impurity sites) and the magnetization enhancement factor is nearly independent of the magnetic field (see Fig. 4 of Ref.<sup>27</sup>). Remarkably, the field-cooled magnetization at a fixed temperature was found to increase with time<sup>27</sup>, implying that the field-cooled magnetization should increase with cooling rate. This is similar to what we have observed in our MWCNTs embedded with ferromagnetic nanoparticles (see Fig. 10). Furthermore, curves 1 and 3 in Fig. 9a also demonstrate that the large magnetization enhancements only occur at temperatures well below the Curie temperatures of the ferromagnetic impurity phases and the enhanced magnetizations get lost above the Curie temperatures (850 K and 1050 K) of the  $\text{Fe}_3\text{O}_4$  and Fe phases, respectively. This is consistent with the fact that ferromagnetically ordered impurities are very effective flux pinning centers<sup>28</sup> and that strong flux pinning causes the HFPME<sup>26</sup>. Therefore, all these unusual magnetic properties can be well explained by the HFPME.

If individual MWCNTs are superconductors, a MWCNT mat should be a granular superconductor. Below a Josephson-coupling temperature, the magnetic response could be paramagnetic or diamagnetic depending on the Josephson-coupling strength and magnetic field<sup>29</sup>. The data shown in Fig. 11 are consistent with the expected magnetic response of a granular superconductor.

If the HFPME interpretation is relevant, one must assume that our MWCNTs should exhibit ultrahigh temperature superconductivity with  $T_c > 1050$  K. This is consistent with a single-particle tunneling gap of about 200 meV, which was identified<sup>16</sup> in a 30-nm MWCNT. Electrical transport data for a MWCNT mat sample were also found to agree with granular superconductivity below the mean-field  $T_c$  of about 700 K. Further, the inelastic scattering rate at room temperature was found to be very large (about 30 meV) in graphite<sup>30</sup>. With the Fermi-velocity of about  $8 \times 10^5$  m/s, one calculates the inelastic mean-free path to be 18 nm in graphite, which is far shorter than that (about 1  $\mu\text{m}$ ) estimated from electrical transport measurement<sup>31</sup>. For individual MWCNTs, the room-temperature mean-free path was determined to be larger than 65  $\mu\text{m}$  (Ref.<sup>32</sup>). These transport data cannot be explained by ballistic transport but are consistent with phase-incoherent room-temperature superconductivity.

#### IV. CONCLUDING REMARK

Because there have been no traditional signatures of bulk superconductivity (e.g., large diamagnetic Meissner effect and the zero-resistance state) in these materials, our interpretation in terms of the HFPME might be questionable. However, since we are not aware of any better explanations based on other physics models, the interpretation based on the HFPME due to ultrahigh temperature superconductivity in MWCNTs should be the most relevant.

**Acknowledgment:** We thank M. Du and F. M. Zhou for the elemental analyses using ICP-MS. Use of the Advanced Photon Source was supported by the U.S. Department of Energy, Office of Science, Office of Basic Energy Sciences, under Contract No. DE-AC02-06CH11357. This work was partly supported by the National Natural Science Foundation of China (10874095) and Y. G. Bao's Foundation.

\* Corresponding should be addressed to gzhao2@calstatela.edu

---

- <sup>1</sup> Z. Y. Meng, T. C. Lang, S. Wessel, F. F. Assaad, and A. Muramatsu, *Nature (London)* **464**, 08942 (2010).
- <sup>2</sup> G. Baskaran and S. A. Jafari, *Phys. Rev. Lett.* **89**, 016402 (2002).
- <sup>3</sup> P. W. Anderson, *Science* **235**, 1196 (1987).
- <sup>4</sup> A. M. Black-Schaffer and S. Doniach, *Phys. Rev. B* **75**, 134512 (2007).
- <sup>5</sup> Y. Kopelevich, P. Esquinazi, J. H. S. Torres, and S. Moehlecke, *J. Low Temp. Phys.* **119**, 691 (2000).
- <sup>6</sup> S. Moehlecke, C. Ho, and M. B. Maple, *Phil. Mag. B* **82**, 1335 (2002).
- <sup>7</sup> A. W. Momburu, H. Pardo, R. Faccio, O. F. de Lima, E. R. Leite, G. Zanelatto, A. J. C. Lanfredi, C. A. Cardoso, and F. M. Araujo-Moreira, *Phys. Rev. B* **71**, 100404(R) (2005).
- <sup>8</sup> P. Esquinazi, D. Spemann, R. Hohne, A. Setzer, K. H. Han, and T. Butz, *Phys. Rev. Lett.* **91**, 227201 (2003).
- <sup>9</sup> J. Cervenka, M. I. Katsnelson, and C. F. J. Flipse, *Nature Physics* **5**, 840 (2009).
- <sup>10</sup> H. Ohldag, P. Esquinazi, E. Arenholz, D. Spemann, M. Rothermel, A. Setzer, and T. Butz, *New J. Phys.* **12**, 123012 (2010).
- <sup>11</sup> K. Antonowicz, *Nature (London)* **247**, 358-360 (1974).
- <sup>12</sup> S. G. Lebedev, *Nucl. Instr. Meth.* **A521**, 22 (2004).
- <sup>13</sup> S. Dusari, J. Barzola-Quiquia, and P. Esquinazi, *J. Sup. Nov. Magn.* **24**, 4012 (2011).
- <sup>14</sup> G. M. Zhao and Y. S. Wang, cond-mat/0111268.
- <sup>15</sup> G. M. Zhao, *Molecular Nanowires and Other Quantum Objects*, A. S. Alexandrov, J. Demsar, and I. K. Yanson, (Eds), (Nato Science Series, Kluwer Academic Publishers, Netherlands, 2004) page 95-106.
- <sup>16</sup> G. M. Zhao, *Trends in Nanotubes Research*, edited by Delores A. Martin (Nova Science Publishers, New York, 2006) page 39-75, and references therein.
- <sup>17</sup> I. Felner and Y. Kopelevich, *Phys. Rev. B* **79**, 233409 (2009).
- <sup>18</sup> J. Wang, P. Beeli, Y. Ren, and G. M. Zhao, *Phys. Rev. B* **82**, 193410 (2010).
- <sup>19</sup> D. Reznik, C. H. Olk, D. A. Neumann, and J. R. D. Copley, *Phys. Rev. B* **52**, 116 (1995).
- <sup>20</sup> W. Gong, H. Li, Z. Zhao, and J. Chen, *J. Appl. Phys.* **69**, 5119 (1991).
- <sup>21</sup> G. F. Goya, T. S. Berquo, F. C. Fonseca, and M. P. Morales, *J. Appl. Phys.* **94**, 3520 (2003).

- <sup>22</sup> J. Wang, W. Wu, F. Zhao, and G. M. Zhao, *Appl. Phys. Lett.* **98**, 083107 (2011).
- <sup>23</sup> S. Gangopadhyay, G. C. Hadjipanayis, B. Dale, C. M. Sorensen, K. J. Klabunde, V. Paefthymiou and A. Kostikas, *Phys. Rev. B* **45**, 9778 (1992).
- <sup>24</sup> O. Cespedes, M. S. Ferreira, S. Sanvito, M. Kociak, and J. M. D. Coey, *J. Phys.: Condens. Matter* **16**, L155 (2004).
- <sup>25</sup> T. D. Cheung, J. S. Kouvel, and J.W. Garland, *Phys. Rev. B* **23**, 1245 (1981); and references therein.
- <sup>26</sup> A. I. Rykov, S. Tajima, and F. V. Kusmartsev, *Phys. Rev. B* **55**, 8557 (1997).
- <sup>27</sup> F. T. Dias, P. Pureur, P. Rodrigues Jr, and X. Obradors, *Phys. Rev. B* **70**, 224519 (2004).
- <sup>28</sup> N. D. Rizzo, J. Q. Wang, D. E. Prober, L. R. Motowidlo, and B. A. Zeitlin, *Appl. Phys. Lett.* **69**, 2285 (1996).
- <sup>29</sup> M. Chandran, *Phys. Rev. B* **56**, 6169 (1997).
- <sup>30</sup> K. Sugawara, T. Sato, S. Souma, T. Takahashi, and H. Suematsu, *Phys. Rev. Lett.* **98**, 036801 (2007).
- <sup>31</sup> S. Dusari, J. Barzola-Quiquia, P. Esquinazi, and N. Garcia, *Phys. Rev. B* **83**, 1225402 (2011).
- <sup>32</sup> P. Poncharal, C. Berger, Y. Yi, Z. L. Wang, W. A. de Heer, *J. Phys. Chem. B* **106**, 12104 (2002).